MATERIALS CHEMISTRY FRONTIERS

CHINESE CHEMICAL SOCIETY

ROYAL SOCIETY OF CHEMISTRY

RESEARCH ARTICLE

View Article Online
View Journal | View Issue

Cite this: *Mater. Chem. Front.*, 2026, **10**, 1990

d^2 ion-doped vacancy-ordered double perovskites as broadband NIR scintillators for radiation detection

Bing-Jun Zhu,[a] Jiacheng Liu,[b] Yang (Michael) Yang,[b] En Ma,[c] Jia-Jun Yan,[a] Heng-Yun Ye*[a] and Le-Ping Miao*[a]

Received 27th January 2026,
Accepted 3rd April 2026

DOI: 10.1039/d6qm00065g

rsc.li/frontiers-materials

Scintillators can convert high-energy X-rays into more easily observable visible-near-infrared (NIR) light, thus showing great application potential in fields such as medical imaging, industrial inspection, and high-energy physics. Current NIR photodiodes exhibit higher photoelectric conversion efficiency than their counterparts operating in the visible light region. Integrating NIR scintillators with NIR optoelectronic conversion devices exhibiting high photoelectric conversion efficiency represents a promising solution for achieving efficient X-ray detection. However, almost all current scintillators are limited to the visible light region or exhibit poor performance. In this work, we achieve efficient NIR scintillation by doping Cs_2ZrCl_6 with d^2 ions. The light yield (LY) of the sample is as high as 51 613 photons MeV^{-1}, and the detection limit is as low as 192 nGy_{air} s^{-1}. The flexible scintillator film with an area of 10 × 10 cm^2 prepared by combining the sample with PDMS can be successfully applied to X-ray imaging. The spatial resolution of the Cs_2ZrCl_6:Mo^{4+}@PDMS scintillator screen was 10 lp mm^{-1}, determined using standard X-ray resolution test panel imaging and MTF = 0.2. This work demonstrates that vacancy-ordered double perovskite is a promising matrix for scintillators and a class of potential optically functional materials.

1. Introduction

X-ray detection is a key technology in various fields such as medical diagnosis, security inspection, nuclear power stations, industrial product inspection, and imaging due to its ability to convert high-energy radiation into easily detectable photons.[1–3] X-ray detection technology is divided into direct and indirect detection. Indirect detection refers to the conversion of high-energy X-rays into photons that can be directly detected using photodetectors through scintillators, which plays the more dominant role in the field due to the advantages of high detection efficiency and low manufacturing cost.[4,5] Among the current photodetectors, the photoelectric conversion efficiency of the avalanche photodiode (APD, 80%), more sensitive to red-NIR light, is much higher than that of the photomultiplier tube (PMT) and the silicon photomultiplier tube (SiPM, 30–40%) that receive signals in the visible light region.[6,7] On the other hand, when the material is used in outdoor portable X-ray imaging systems, NIR light can effectively avoid signal crosstalk with visible light. Therefore, to improve optical and scintillation signal detection, it is of great significance to develop efficient NIR luminescent and scintillator materials.[8–12]

Currently, the luminescence peaks of most scintillators are confined to the visible light region.[13,14] The few scintillator materials that can achieve NIR luminescence properties are either activated by rare earths (RE) or realized in classical lead-based halide perovskites. The complex energy levels of RE enable them to produce light in multiple colors from visible to NIR, but the characteristic narrow-band luminescence makes it difficult to form continuous broadband luminescence in the NIR region.[15–17] Previous reports have shown that molecular complexes containing Mo^{4+}, Re^{5+}, and Os^{6+} ions with a d^2 electron configuration can exhibit NIR luminescence, but with low luminescence efficiency.[18] NIR radiation originates from d–d electron transitions of metal ions. There are few reports of Mo^{4+} or W^{4+} doping in halide perovskites.[19] For example, ultra-broad NIR emission has been reported by doping Mo^{4+} or W^{4+} into $Cs_2Na_{0.95}Ag_{0.05}BiCl_6$ double perovskite.[20] Bi^{3+}/Mo^{4+} co-doped $Cs_2Ag_{0.6}Na_{0.4}InCl_6$ double perovskite simultaneously produces

[a] *Chaotic Matter Science Research Center, International Institute for Innovation, Jiangxi University of Science and Technology, Nanchang, 330013, P. R. China. E-mail: hyye@seu.edu.cn, miaoleping@jxust.edu.cn*
[b] *College of Optical Science and Engineering & State Key Laboratory of Extreme Photonics and Instrumentation, Zhejiang University, Hangzhou, 310000, P. R. China*
[c] *Xiamen Key Laboratory of Rare Earth Photoelectric Functional Materials, Xiamen Institute of Rare Earth Materials & Fujian Institute of Research on the Structure of Matter, Chinese Academy of Sciences, Xiamen, 361000, P. R. China*

warm white light and NIR emission. These studies were limited to achieving broadband NIR luminescence through d^2 ion doping and did not consider the excellent NIR scintillation properties that can be obtained through d^2 ion-doped halides. The broadband NIR scintillation characteristics of d^2 ions, combined with the high photoelectric conversion efficiency of APD, are expected to offer significant advantages in X-ray imaging.

It is also crucial to select the appropriate carrier matrix for the activation center. Currently, scintillator materials are mostly made of lead-based, copper-based, RE, and other compounds, but they have disadvantages such as toxicity, easy oxidation to a higher valence state, and hygroscopicity, which hinder their large-scale application.[21–23] Vacancy-ordered perovskites can not only avoid the above risks but also have relatively isolated octahedral groups, which can inhibit non-radiative cross-relaxation.[24,25] Cs_2ZrCl_6 is a stable and environmentally friendly vacancy-ordered double perovskite material with a wide bandgap, which does not interfere with the optical properties of dopants. Therefore, Cs_2ZrCl_6 vacancy-ordered double perovskites are considered to be satisfactory scintillator matrix materials.[13,26]

In this work, we successfully synthesized Mo^{4+} and W^{4+} ion (d^2 ion) doped Cs_2ZrCl_6 vacancy-ordered double perovskite single crystals *via* the hydrothermal method. The phase purity, chemical composition, and ion valence of the samples were characterized by X-ray diffraction (XRD), scanning electron microscopy (SEM), and X-ray photoelectron spectroscopy (XPS). The optical and scintillation properties of d^n ion-doped Cs_2ZrCl_6 were investigated by absorption, spectroscopies, and density functional theory (DFT) simulations, and its emission mechanism was explained using the Tanabe–Sugano plot combined with low-temperature photoluminescence (PL) spectroscopies. The prepared sample was found to have excellent X-ray absorption capacity and high light yield (LY). Therefore, a large-area flexible scintillator screen was prepared by mixing Cs_2ZrCl_6:Mo^{4+} and polydimethylsiloxane (PDMS). The spatial resolution of the scintillation screen was quantified using standard X-ray resolution test panels and a transfer modulation function (MTF) based on the slanted-edge method. The prepared scintillator screen was successfully applied to X-ray imaging.

2. Experimental

The samples are prepared using the simple hydrothermal reaction method. Detailed sample preparation conditions and performance characterization are provided in the SI.

3. Results and discussion

3.1. Structural and morphological characterization

The corresponding vacancy-ordered structure is formed by removing half of the B^{2+} cations from the conventional ABX_3 perovskites, and the remaining $[BX_6]^{2-}$ groups are spaced by the A-site cations in the void. A large number of B vacancies can affect the migration and recombination processes of charge carriers, which may lead to unexpected luminescence effects. Mo^{4+}/W^{4+}-doped Cs_2ZrCl_6 millimeter-scale single crystals were synthesized *via* a hydrothermal method (Fig. S1b). Fig. 1a

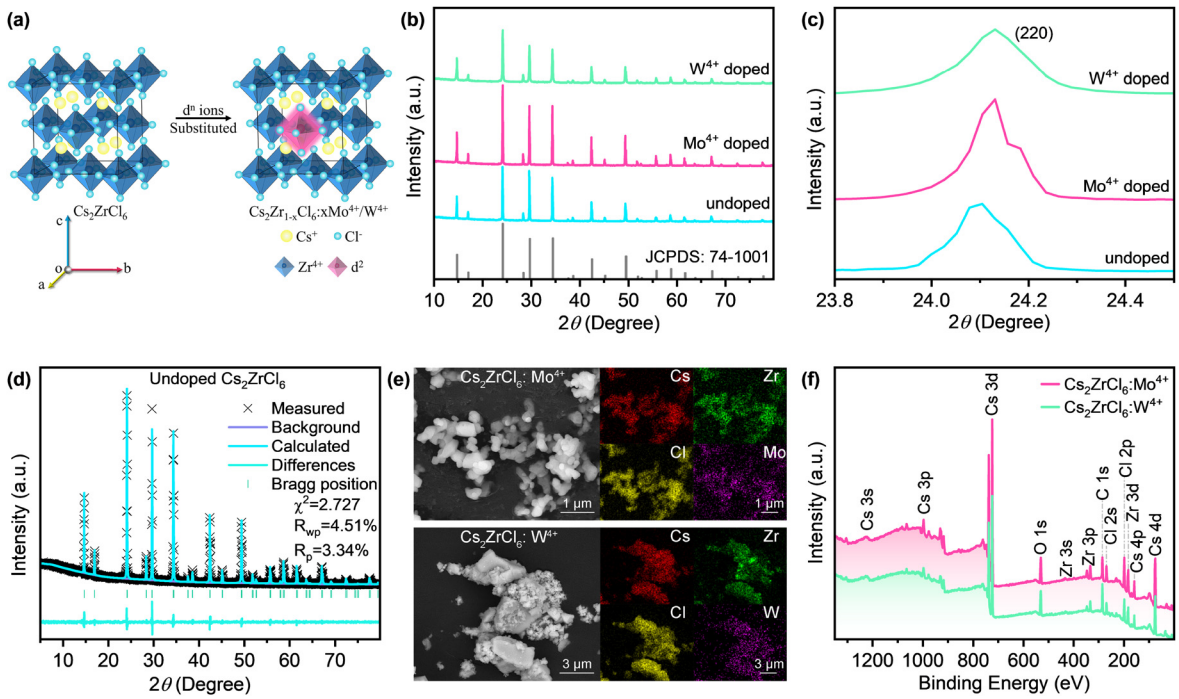

Fig. 1 (a) Schematic diagram of d^2 ion substitution in the Cs_2ZrCl_6 lattice. (b) XRD patterns and (c) local magnification near the (220) crystallographic plane diffraction peak of undoped and Mo^{4+} (15 mol%)/W^{4+} (15 mol%)-doped Cs_2ZrCl_6. (d) Rietveld refinement of XRD patterns of Cs_2ZrCl_6. (e) SEM images and elemental mapping and (f) XPS spectra of Cs_2ZrCl_6:Mo^{4+} (15 mol%)/W^{4+} (15 mol%).

shows the expected crystal structure and doping mechanism of the prepared d^2 ion-doped Cs_2ZrCl_6. Isolated $[ZrCl_6]^{2-}$ octahedra and cavities are arranged alternately in three-dimensional space to form a vacancy-ordered structure, where $a = b = c$ and $\alpha = \beta = \gamma = 90^\circ$. Fig. 1b shows the XRD pattern of the undoped and Mo^{4+}/W^{4+}-doped Cs_2ZrCl_6 and the standard diffraction peak pattern of Cs_2ZrCl_6 (JCPDS no. 74-1001). The diffraction peaks of all samples are consistent with the standard cubic crystal structure (space group: $Fm\bar{3}m$), demonstrating that the doped d^2 ions are well dispersed in the Cs_2ZrCl_6 matrix without forming new impurity phases. Due to the same valence state and similar coordination number (CN) and ionic radius (R), Mo^{4+} (CN = 6 and R = 0.65 Å) and W^{4+} (CN = 6 and R = 0.66 Å) ions will replace the position of Zr^{4+} (CN = 6 and R = 0.72 Å) to form $[MoCl_6]^{2-}/[WCl_6]^{2-}$ octahedra.[27] As impurity ions enter the lattice, the unit cell parameters of the crystal gradually decrease, causing the diffraction peak of the sample to move toward a larger angle (Fig. 1c), which further proves that the smaller doped ions replace the larger Zr^{4+} ions in the Cs_2ZrCl_6 lattice.

Rietveld refinement was used to further extract information from the XRD patterns. The refinement results (variance $\chi^2 < 3$) of undoped (Fig. 1d) and Cs_2ZrCl_6:Mo^{4+} (15 mol%)/W^{4+} (15 mol%) (Fig. S2a and b) indicate that the data are credible. The experimental data and simulated data are in good agreement, with the values of residual least-squares refinement and weighted residue both $< 5\%$. The results of Rietveld refinement verified the overall phase purity of all samples in powder form.

The SEM image shows that the sample is composed of irregularly sized amorphous tiny particles, whose size is distributed in the range of 10 nm to the micrometre scale. Energy dispersive spectroscopy (EDS) mapping shows the uniform distribution of Cs, Zr, Cl, Mo, and W elements in the compound (Fig. 1e), which also proves that the d^2 ions are randomly substituted and uniformly dispersed on the Zr^{4+} lattice sites.

XPS is used to reveal the composition and elemental valence states of compounds. XPS spectra prove the presence of Cs, Zr, and Cl elements in d^2 ion-doped Cs_2ZrCl_6 samples (Fig. 1f).[24] In the high resolution XPS spectrum, the binding energy peaks located near 232.01 and 235.09 eV correspond to Mo^{4+} $3d_{5/2}$ and Mo^{4+} $3d_{3/2}$, and two peaks at 35.48 and 37.70 eV are assigned to W^{4+} $4f_{7/2}$ and $4f_{5/2}$, respectively, which effectively proves the existence of the +4-oxidation state of the doped Mo and W (Fig. S2f).[28–30] A comparison between the elemental ratios determined by the XPS peak area ratio and the actual sample feed ratio showed that only about half of the d^2 ions were successfully doped (Tables S1 and S2). It is worth noting that the binding energies of Cs, Zr, and Cl in the XPS spectrum of W^{4+}-doped Cs_2ZrCl_6 are all higher than those of the Mo^{4+}-doped sample (Fig. S2c–e). This is because $R_{W^{4+}} > R_{Mo^{4+}}$, and the W^{4+}-doped sample has a larger unit cell parameter, which leads to a lower electron cloud density, resulting in a higher binding energy for its XPS peak.[31]

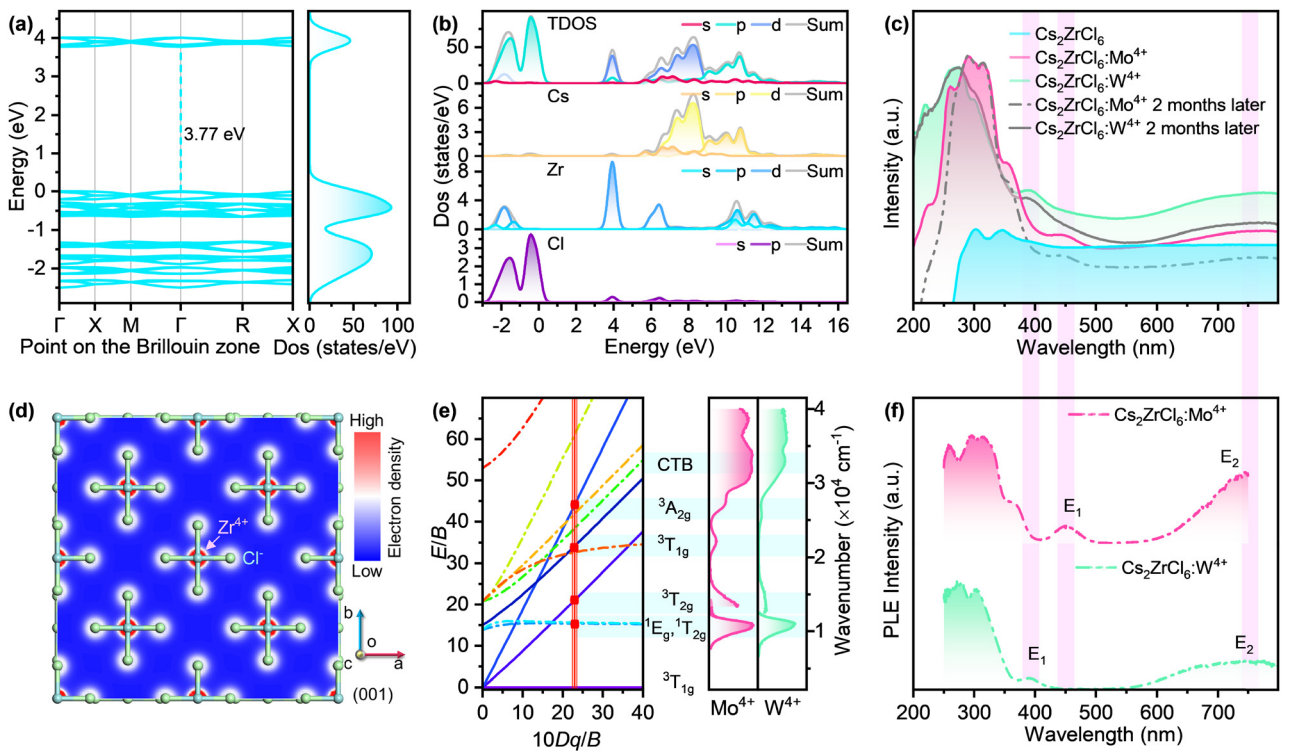

Fig. 2 (a) Electronic band structure and (b) atom PDOS of Cs_2ZrCl_6. (c) UV-visible absorption spectra of undoped and Mo^{4+} (5 mol%)/W^{4+} (15 mol%)-doped Cs_2ZrCl_6. (d) Electron density isosurface at the (001) facet of Cs_2ZrCl_6. (e) Tanabe–Sugano diagram of the d^2 electron configuration in an octahedral crystal field environment and the corresponding PL(E) spectra of Mo^{4+}/W^{4+}-doped Cs_2ZrCl_6. (f) PLE spectra of Cs_2ZrCl_6:Mo^{4+} (5 mol%)/W^{4+} (15 mol%).

3.2. Optical performance

First-principles-based DFT was used to investigate the electronic properties of the samples. The electronic band structure and atomic partial density of states (PDOS) were calculated to explore the effects of Mo^{4+} and W^{4+} doping on pristine Cs_2ZrCl_6. The electronic band structure shows that both the valence band maximum (VBM) and the conduction band minimum (CBM) are located at the center of the Brillouin zone (Γ point), indicating that the material is a direct bandgap semiconductor (Fig. 2a). The samples introduced with Mo^{4+} and W^{4+} are still direct bandgap semiconductors, but a new electron distribution is generated in the middle of the bandgap, resulting in the reduction of the bandgap from 3.77 eV to 2.83 eV and 3.39 eV (Fig. S3a and d), respectively. It can be observed from the PDOS (Fig. 2b) that for the undoped Cs_2ZrCl_6 sample, the VBM mainly comes from the contribution of Cl 3p, while the CBM originates from Zr 4d. The electronic band structure mainly comes from the contribution of the $[ZrCl_6]^{2-}$ group, and the contribution of Cs^+ ions to the electronic band structure is mainly in the depth of the band rather than near the band gap. The CBM of Mo^{4+} and W^{4+}-doped Cs_2ZrCl_6 is mainly derived from Zr 4d and Mo 4d as well as Zr 4d and W 5d states, respectively (Fig. S3b and e). The VBM is still composed of Cl 3p states. The introduction of d^2 ions modulates the band gap of Cs_2ZrCl_6 and also leads to changes in the optical behavior, which is discussed below.

We next discussed the effect of d^2 ion doping on the optical properties of Cs_2ZrCl_6. The UV-visible absorption spectra of the samples are shown in Fig. 2c. For the undoped Cs_2ZrCl_6 matrix, a constant weak absorption appears after 260 nm. In contrast, the d^2 ion-doped sample exhibits a strong absorption peak in the range of 200–400 nm, whose electronic structure is dominated by isolated $[MoCl_6]^{2-}$/$[WCl_6]^{2-}$ groups. Accordingly, the absorption band of the doped sample originates from the d–d transition of d^2 ions. Since the absorption peaks in the visible light range of the d^2 ion-doped samples are concentrated near red light and blue light, this corresponds well to the macroscopic green color of the doped samples (Fig. S1b). Notably, the crystal exhibited no change in optical properties after being exposed to air for a period without special protection, indicating that the valence state of the excitation centers remained unchanged. The optical band gap of the sample was calculated by the Tauc-plot method (formula (S1)), as shown in Fig. S3c, showing that the doping of Mo^{4+} and W^{4+} resulted in a decrease in the band gap. The results show that the band gap values of pure, Mo^{4+} (5 mol%), and W^{4+} (15 mol%) doped Cs_2ZrCl_6 are 3.74, 3.17, and 3.48 eV, respectively, which are correlate well with the values predicted by DFT calculations.

Two-dimensional electronic isosurfaces are used to intuitively display the mechanism of charge energy transfer within the crystal. The Zr^{4+} ions in Cs_2ZrCl_6 are almost completely ionized, and the Zr–Cl bond exhibits ionic bond characteristics (Fig. 2d).[32] This property is not changed after Mo^{4+}/W^{4+} replaces Zr^{4+} in the crystal (Fig. S3g and h). The difference is that the electron cloud density of the doped site is significantly higher than that of its undoped counterpart, while the luminescence performance of the sample is closely related to the electron density. The changes in crystal band structure and electron distribution caused by d^2 ion doping will affect the optical properties of the sample.

In order to probe the optical properties of the samples, the PL spectra for different d^2 ion doping concentrations were measured and are shown in Fig. S3j and k. As the doping amount increases, the intensity of the NIR peak first increases gradually, and after reaching the maximum intensity, it begins to decrease due to concentration quenching caused by energy migration between d^2 ions (Fig. S3i). The shape and position of the NIR peaks were not observed to change over the entire concentration range. From the perspective of optical performance, the optimal doping concentrations of Mo^{4+} and W^{4+} are 5 mol% and 15 mol%, respectively. The PL and PL excitation (PLE) spectra of the samples with the optimal doping concentration are shown in Fig. S3f and Fig. 2f. The peak positions in the PLE spectrum correspond well to the absorption peaks. By comparing the Tanabe–Sugano diagram (Fig. 2e), it can be concluded that the PLE peaks at 355 nm, 450 nm, and 760 nm of Cs_2ZrCl_6:Mo^{4+} (5 mol%) are attributed to the $^3A_{2g}(F)$–$^3T_{1g}(F)$, $^3T_{1g}(P)$–$^3T_{1g}(F)$, and $^3T_{2g}(F)$–$^3T_{1g}(F)$ transitions, respectively.[33–36] The PLE peaks at 393 nm and 790 nm of Cs_2ZrCl_6:W^{4+} (15 mol%) are considered to be $^3A_{2g}(F)$–$^3T_{1g}(F)$ and $^3T_{2g}(F)$–$^3T_{1g}(F)$ transitions. Additionally, their strong PLE bands at lower wavelengths originate from the charge transfer bands (CTB) between Cl^- and d^2 ions. The gradual blue shift of the CTB in samples doped with Mo^{4+} and W^{4+} is due to the increase in their electronegativity difference.[29] Undoped Cs_2ZrCl_6 has an intrinsic weak blue luminescence, which originates from the exciton emission of the $[ZrCl_6]^{2-}$ group.[32] For both Mo^{4+} and W^{4+}-doped samples, broadband NIR peaks extending from 800 nm to around 1300 nm appeared, centered at 925 and 914 nm, and the full width at half maximum (FWHM) reached 175 and 169 nm, respectively. The extended non-Gaussian luminescence peak at long wavelength is due to the multiple radiative transitions of the lowest excited state of the octahedrally coordinated d^2 ions to the ground state sublevel.[29] Based on DFT calculations and experimental results, the origin of PL of d^2 ion-doped Cs_2ZrCl_6 was proposed (Fig. S4a). Under ultraviolet excitation, electrons are transported from the Cs_2ZrCl_6 ground state to the conduction band (CB) and reach the edge of the CB after nonradiative relaxation. In an undoped system, this energy is directly used to produce visible light emission. However, in d^2 ion-doped systems, this energy is further transferred to newly formed energy levels, resulting in broadband NIR emission.

In an octahedral coordination environment and considering the lattice phonon–electron interaction, the luminescence behavior of transition metal (TM) ions can be described by combining the Tanabe–Sugano diagram (Fig. 2e) with the configuration coordinate curve. At different Dq/B values, the energy of ^1E_g/$^1T_{2g}$ is almost constant, while $^3T_{2g}$, $^3T_{1g}$, and $^3A_{2g}$ have larger energy differences. This resulted in extremely similar PL spectra for the two samples doped with Mo^{4+} and W^{4+}, while the peak positions of the PLE spectra changed. After comparison, it was found that the experimental data of the Mo^{4+} and W^{4+}-doped samples were in excellent agreement with the Tanabe–Sugano diagram at the position of $10Dq/B$ = 23. The crystal field splitting energies

(10*Dq*) of Mo^{4+} and W^{4+} are 15 318 cm^{-1} and 14 789 cm^{-1}, respectively. The detailed calculation process is shown in the SI. Doping with Mo^{4+} and W^{4+} of large atomic numbers leads to strong spin–orbit coupling (SOC), which causes asymmetric vibrations in the fluorescence process and partially relaxes the Laporte selection rule.[20] The NIR peaks of Mo^{4+} and W^{4+} both originate from the $^1E_g(D)/^1T_{2g}(D) \rightarrow {}^3T_{1g}(F)$ transition, as shown in Fig. 2e.

Additionally, the PL lifetime of the samples was also investigated to further reveal the luminescence properties. The reduced symmetry of the TM octahedral environment and SOC will break the d–d transition selection rule, which is beneficial for the improvement of optical properties. As shown in Fig. S3l, the fluorescence decay curve for the Mo^{4+}-doped sample was measured at an emission wavelength of 925 nm under excitation at 295 nm, whereas that for the W^{4+}-doped sample was obtained by measuring the emission at 914 nm under excitation at 270 nm. For the Mo^{4+}-doped sample, two components with comparable decay times are 68.61 and 68.60 μs, and their proportions are close, accounting for 58% and 42%, respectively (fitted using formulas (S2) and (S3)). Similarly, the proportions of the two equivalent components (34.52 and 34.6 μs) in the lifetime of the W^{4+}-doped sample are 52% and 48%, respectively. The lifetimes of the different components are almost the same, indicating that the luminescence of the sample is derived from multiple radiation transitions of splitting sub-energy levels from the same source, rather than a mixture of luminescence from different mechanisms. The average lifetimes of Mo^{4+} and W^{4+}-doped samples are 68.6 and 35.4 μs, respectively, which are within the order of magnitude of ions with a d^2 electron configuration of the TM.[37] Additionally, W^{4+} decays faster than Mo^{4+}, which is because the larger atomic number leads to a stronger SOC. SOC will relax the parity selection rule of the d–d transition and thus enhance the radiation probability, resulting in a shortened lifetime.[29,30]

Lattice phonons can significantly affect the optical properties of TM ions with exposed d^2 external electron shells. Accordingly, temperature is a crucial parameter that affects the PL phenomenon of the samples. To obtain better spectral resolution, the temperature dependence spectra of Cs_2ZrCl_6:Mo^{4+} (5 mol%) in the range of 80–560 K were measured as shown in Fig. 3a. The NIR peak of the sample is non-Gaussian symmetric at room temperature, with multiple shoulders on the long wavelength side. At low temperatures, the peak splitting becomes more obvious, with two peaks of relatively high intensity. This phenomenon indicates that the broadband peak originates from multiple transitions, and the temperature-induced peak broadening contributes to the formation of the broadband NIR peak. As the temperature increases, the peak positions of the split peaks in the observable temperature range remain almost unchanged, and the overall PL intensity gradually decreases. In fact, due to the effects of SOC, lattice tetragonal distortion, and Cl 3p state coupling, the ^1E_g and $^1T_{2g}$ excited states and $^3T_{1g}$ ground state energy levels are split into multiple energy levels.[29] As shown in Fig. S4b, the NIR peak is actually composed of many peaks. It is worth mentioning that here the 1–8 fitting

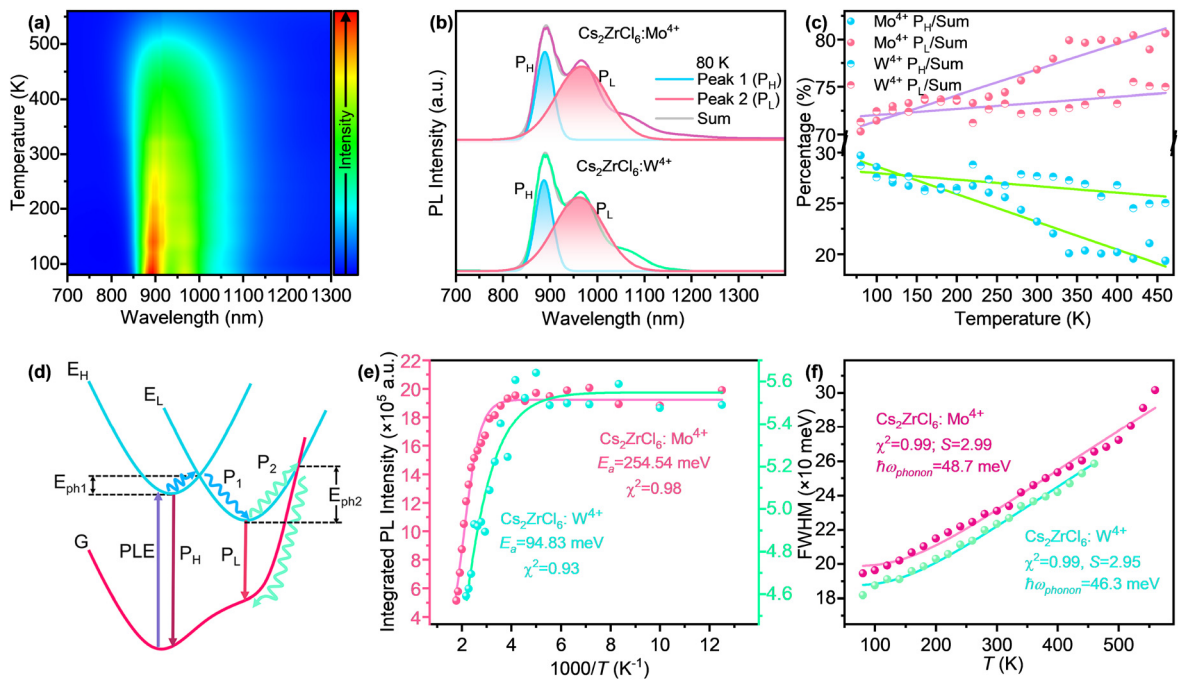

Fig. 3 (a) Pseudo-color plot of the temperature-dependent PL spectra (excited at 295 nm) for Cs_2ZrCl_6:Mo^{4+} (5 mol%) measured in the range of 80–560 K. (b) Deconvolution of the spectrum of Cs_2ZrCl_6:Mo^{4+} (5 mol%)/W^{4+} (15 mol%) measured at 80 K. (c) The variation of the integrated area ratio of P_H and P_L with temperature and the corresponding linear fitting. (d) Thermal quenching schematic of d^2 ion luminescence in the Cs_2ZrCl_6 lattice. (e) Integrated PL emission intensity as a function of the reciprocal of temperature and its fitting results. (f) FWHM as a function of temperature and corresponding fitting result.

peaks cannot be specifically assigned to which transition each one corresponds, but they only illustrate that they arise from transitions between multiple sub-energy levels. As shown in Fig. 3b, in order to reveal the change in the shape of the NIR peak during the temperature change process, the low-temperature spectrum of Cs_2ZrCl_6:Mo^{4+} (5 mol%)/W^{4+} (15 mol%) was deconvoluted into high-energy peaks (P_H) and low-energy peaks (P_L). As the temperature increases, the integrated intensity ratio of P_H decreases, while the ratio of P_L increases (Fig. 3c). A simplified energy level diagram is used to explain the changing trend of the relative intensity of different peaks during temperature change (Fig. 3d). Multiple transition peaks are simplified into a high energy peak (P_H) returning to the ground state (G) *via* the high energy level (E_H) and a low energy peak (P_L) returning to the ground state *via* the low energy level (E_L). Electrons at E_H can obtain phonon energy (E_{ph1}) by coupling with lattice phonons and reach low energy levels through a non-radiative decay path (P_1) to complete a radiative transition. As the temperature increases, the increase in lattice phonons is positive for path P_1, which explains the trend of P_H and P_L in Fig. 3c. Analogously, excited electrons can achieve electron–phonon coupling to obtain phonon energy (E_{ph2}) and achieve de-excitation through non-radiative pathways (P_2). The decrease in the intensity of the NIR peak with increasing temperature is due to the increase in the proportion of electrons returning to the ground state *via* the non-radiative pathway. The temperature-dependent PL spectra of 15 mol% Cs_2ZrCl_6:W^{4+} exhibit the same peak splitting and thermal quenching phenomena as those of the Mo^{4+}-doped sample (Fig. S4c).

The NIR peaks disappear around 500 K, showing excellent resistance to thermal quenching of luminescence. Mo^{4+} and W^{4+}-doped samples can maintain 79.6% and 92.3% of the room temperature (27 °C) PL integrated intensity at 150 °C, respectively. The thermal quenching behavior of the PL peak of the sample at varying temperatures can be evaluated using the activation energy of thermal quenching (E_a), which is calculated using formula (S4), and the results are shown in Fig. 3e. The higher E_a means that electrons require more phonon assistance to de-excite through non-radiative pathways, while a lower activation energy will result in the luminescence of the sample having more severe thermal quenching behavior. The value of E_a follows the order Cs_2ZrCl_6:Mo^{4+} (254.54 meV) > Cs_2ZrCl_6:W^{4+} (94.83 meV), as shown in Fig. 3e. This relatively high E_a is attributed to the fact that the photogenerated excitons are confined in isolated octahedral units in the zero-dimensional (0D) structure.[38,39] The E_a of the sample is higher than the thermal energy at room temperature (RT, 26 meV), and the energy barrier is higher than that at RT, which ensures that the excitons can effectively recombine at RT.[40] Additionally, the FWHM of the NIR PL peak of Cs_2ZrCl_6:Mo^{4+}/W^{4+} gradually increases with the increasing temperature (Fig. 3f). The variation of FWHM with temperature of d^2 ion doped Cs_2ZrCl_6 is due to the influence of lattice phonons. In order to further explore the electron–phonon coupling of the Mo^{4+}/W^{4+}-doped sample, according to Toyozawa's theoretical analysis, the Huang–Rhys factor S of the sample was calculated to characterize the electron–phonon coupling strength (formula (S5)). The variation of FWHM with temperature of Mo^{4+} and W^{4+}-doped samples can be well fitted with the theoretical curve (Fig. 3f), and their S values are 2.99 and 2.95, respectively. This small electron–phonon coupling coefficient indicates that the bond length changes very little during the entire temperature change process, and the structural rigidity is relatively high. Simultaneously, this magnitude of S also indicates that the NIR PL originates from d–d transitions, which corroborates the previous conclusions, rather than from the self-trapped exciton (STE).[30] Additionally, STE emission does not exhibit the phenomenon of spectral splitting into multiple vibrational coupling peaks at low temperatures.

3.3. Scintillation performance and applications

The sample also exhibits excellent NIR radioluminescence (RL) characteristics under X-ray irradiation, making it a promising X-ray detector and imaging scintillator. Fig. 4a shows the mechanism of X-ray scintillation in lead-free halide vacancy-ordered double perovskite. The high-energy X-rays first interact with the heavy atoms in the lattice and then eject massive hot electrons mainly through the photoelectric effect and inelastic Compton scattering. These generated thermal carriers (holes and electrons) undergo thermalization into low-energy excitons within an ultrafast time scale, and then the electrons and holes relax to the CB and valence band (VB) of the matrix, respectively. The CB electrons and the VB holes will recombine to produce radiative transitions directly or through the energy level of the doped luminescent ions. The latter process completely overlaps with the path of the PL radiation process.

d^2 ion-doped Cs_2ZrCl_6 can be used as a broadband NIR scintillator. The scintillation peaks of Cs_2ZrCl_6 doped with different Mo^{4+}/W^{4+} concentrations under X-ray irradiation have the same position and shape, but the intensity is different. As the d^2 ion doping concentration increases, the scintillation peak intensity of the sample increases, reaches a maximum value at the concentration of 15 mol%, and then begins to decrease (Fig. S5a–c). In addition, the normalized PL and RL spectra of the samples are almost completely overlapped (Fig. S5d), indicating that the exciton recombination pathways of the two processes are the same. Since the scintillation process involves various complex mechanisms, including the attenuation, absorption, and conversion of X-rays by the sample, the optimal doping concentration for scintillation differs from that for photoluminescence. The RL lifetime of the sample is presented in Fig. S6a, which is significantly higher than its PL lifetime. This may be attributed to the fact that X-rays primarily generate a large number of high-energy electrons through ionization excitation, and then the exciton generation process ultimately resembles that in electroluminescence, leading to recombination *via* rapid singlet pathways.[13,41,42] This indicates that PL and RL reach the d^2 ions *via* different pathways, exhibiting similar emission peak characteristics but different lifetimes. The total attenuation coefficient is used to evaluate the X-ray absorption capacity of the sample and thus reflects its potential as a scintillator. According to the photon cross-section database, the absorption coefficient of Cs_2ZrCl_6:Mo^{4+}/W^{4+} is compared with that of several classical scintillators over a wide photon energy range,

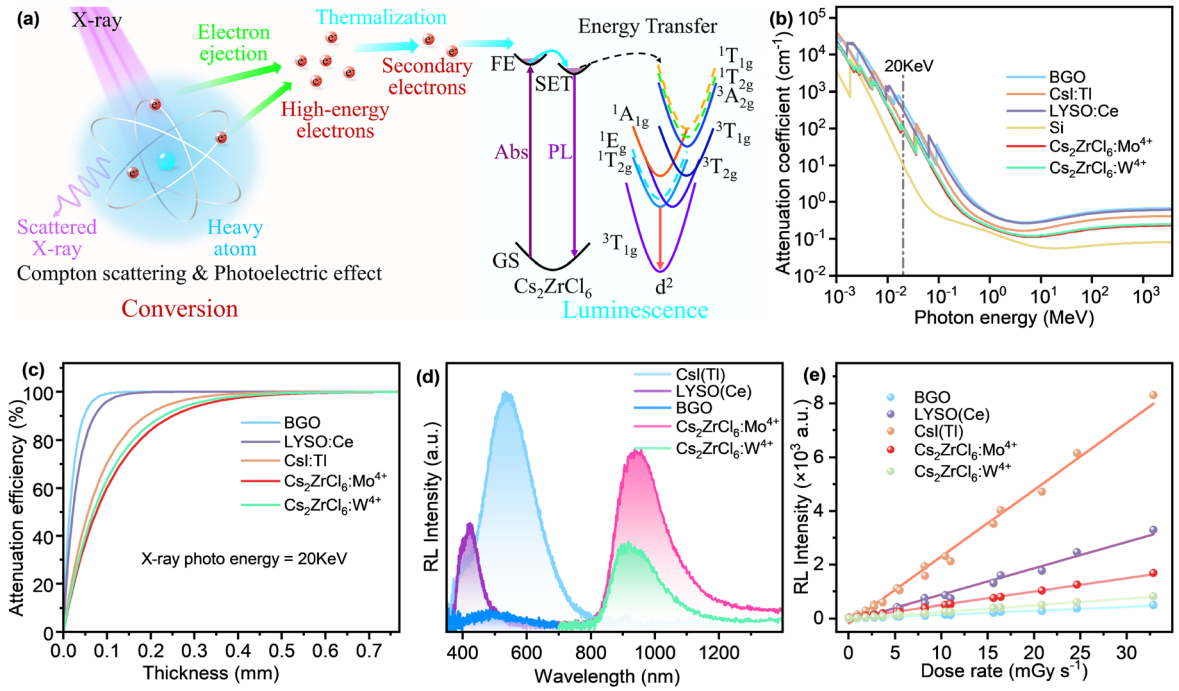

Fig. 4 (a) X-ray scintillation mechanism in lead-free halide double perovskites. (b) X-ray linear absorption coefficient, (c) X-ray attenuation efficiency (X-ray photon energy = 20 KeV), (d) RL spectra (X-ray tube voltage = 20 kV; dose rate = 3.7 mGy_{air} s^{-1}), and (e) RL intensity as a linear function of dose rate of $Cs_2ZrCl_6:Mo^{4+}$ (15 mol%)/W^{4+} (15 mol%) and several common scintillators.

and the results are shown in Fig. 4b.[43] $Cs_2ZrCl_6:Mo^{4+}/W^{4+}$ is entirely composed of light atoms, so its absorption coefficient is slightly lower than that of LYSO:Ce and BGO, but comparable to that of CsI:Tl and much higher than that of Si. The total attenuation coefficient takes into account the density of the sample and is only related to the sample thickness. Therefore, the relationship between the X-ray attenuation efficiency and the sample thickness is calculated to characterize the X-ray absorption capacity of the sample in practical applications (Fig. 4c and formulas (S6) and (S7)). The result shows that a sample with a thickness of only 0.5 mm can completely absorb 20 keV X-ray. This indicates that the d^2 ion-doped samples have considerable X-ray absorption capabilities.

The LY was used to evaluate the scintillation performance of the samples. By comparing with commercial scintillator CsI:Tl, the LY values of $Cs_2ZrCl_6:Mo^{4+}$ (15 mol%) and $Cs_2ZrCl_6:W^{4+}$ (15 mol%) are determined to be 51 613 photons MeV^{-1} and 20 023 photons MeV^{-1}, respectively (Fig. 4d and formula (S8)).[44] The excellent scintillation performance of the sample is attributed to the higher charge transfer and radiative recombination efficiencies of the new pathway after d^2 ion doping.

The linear response behavior of the sample to the X-ray dose rate can be used to evaluate its sensitivity to the X-ray. The intensity of the RL spectra of $Cs_2ZrCl_6:Mo^{4+}/W^{4+}$ and commercial scintillators at different doses of X-rays changes significantly (Fig. S5e–i). The intensity changes of all samples can conform to the linear relationship with the increase of dose rate from 0.019 mGy_{air} s^{-1} to 32.86 mGy_{air} s^{-1}. d^2 ion-doped Cs_2ZrCl_6 has a larger slope (Fig. 4e), which means that it will show more obvious differences between objects of different materials when this material is used for imaging, thus achieving better imaging results.

A low detection dose rate is advantageous in the practical application of scintillators. Taking into account the influence of the instrument background signal, the minimum detection limits of $Cs_2ZrCl_6:Mo^{4+}/W^{4+}$ were determined to be 192 and 546 nGy_{air} s^{-1}, respectively, at the signal-to-noise ratio (SNR) of 3 (Fig. S5l). Such a low detection limit is already far below the dose rate required for medical X-ray diagnosis (5.5 μGy_{air} s^{-1}), indicating that this sample has great application potential in the field of NIR scintillation.[45]

The temperature-dependent RL spectra of $Cs_2ZrCl_6:Mo^{4+}$ and $Cs_2ZrCl_6:W^{4+}$ have similar changing trends to the temperature-dependent PL spectra. The peak position does not change within the temperature range, and the peak intensity does not significantly weaken until above 500 K (Fig. S5j and k). Additionally, X-ray fatigue stability is another important factor that limits the use of metal halide scintillators. The irradiation stability of the scintillator was evaluated by detecting the spectral intensity of X-rays being switched on/off over one hour. $Cs_2ZrCl_6:Mo^{4+}$ exhibits excellent radiation stability (Fig. S6b). Under repeated on–off irradiation at a high X-ray dose rate of 3.7 mGy_{air} s^{-1} over 1 hour, it still maintains 95% of the initial RL intensity, with a total dose of 6.66 Gy_{air}, which is equivalent to 33 300 chest X-ray examinations (0.2 mGy_{air}).[46]

Since Mo^{4+}-doped samples have better scintillation properties, they are mixed with PDMS to make flexible films for scintillation imaging. Fig. 5a shows a large-area flexible scintillator screen with an area of 10 × 10 cm^2 prepared by spin coating. The $Cs_2ZrCl_6:Mo^{4+}$@PDMS flexible film has extremely

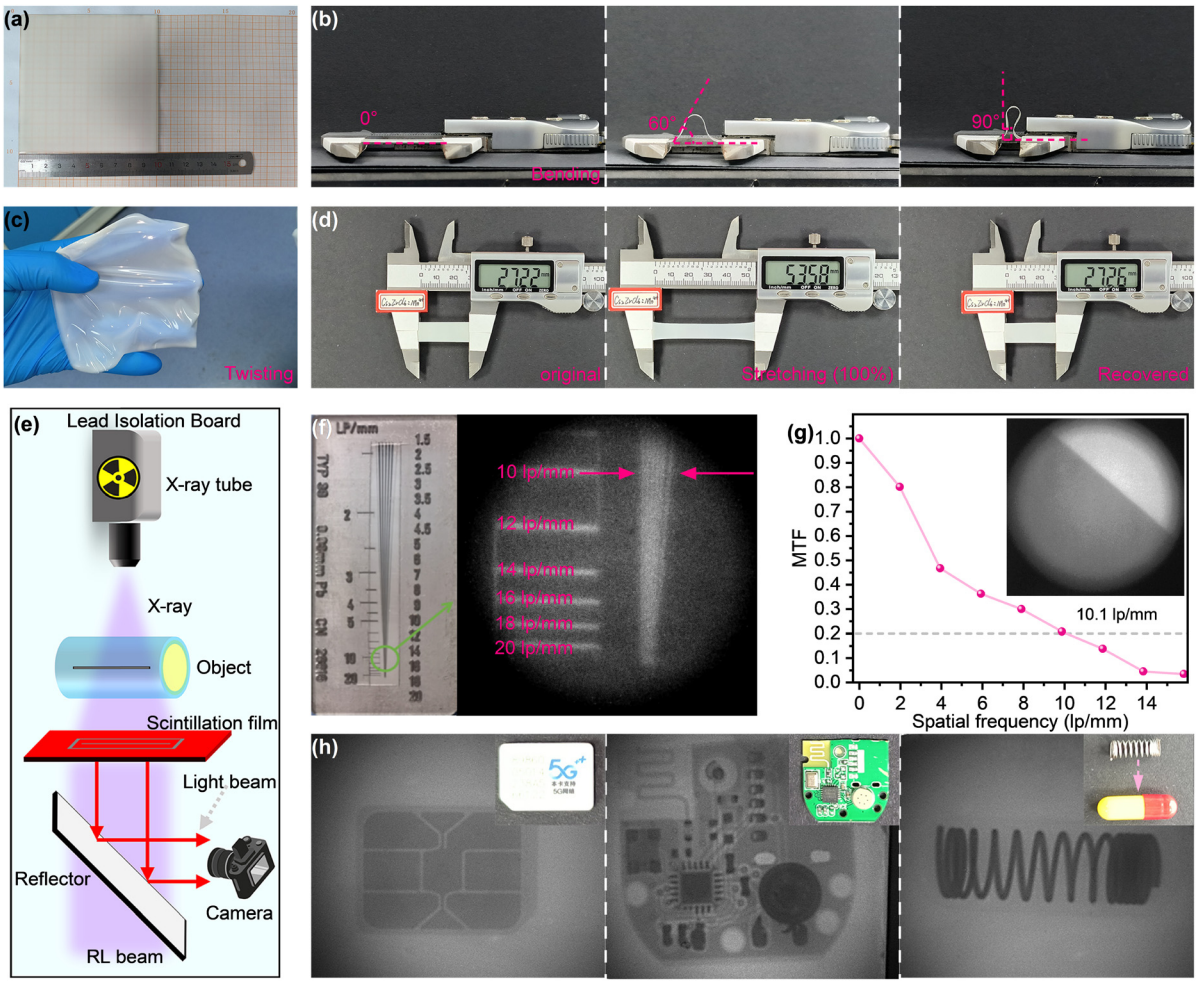

Fig. 5 (a) Images of the large-area flexible scintillation screen that have not been cropped or modified. (b) Photographs of the Cs_2ZrCl_6:Mo^{4+}@PDMS flexible film at different bending angles. (c) Photograph of the Cs_2ZrCl_6:Mo^{4+}@PDMS thin film at twisting mechanical deformations. (d) Photographs of the Cs_2ZrCl_6:Mo^{4+}@PDMS flexible film with different stretching lengths. (e) Schematic diagram of a homemade X-ray imaging system. (f) Photographs of a standard X-ray resolution test pattern plate taken in the bright field and obtained through the Cs_2ZrCl_6:Mo^{4+}@PDMS scintillation screen. (g) The MTF curves of the scintillation screen, and the inset shows the photograph of the corresponding X-ray edge image. (h) Bright-field and X-ray images of objects.

high flexibility and can be bent 90° to maintain its original shape without breaking (Fig. 5b). The flexible film can still be restored to its original state after being twisted or elongated more than 100% (Fig. 5c and d and formula (S9)). To achieve X-ray imaging using Cs_2ZrCl_6:Mo^{4+}@PDMS as the scintillator, a homemade optical system was built, as shown in Fig. 5e. Imaging results from standard X-ray resolution test panels based on the Cs_2ZrCl_6:Mo^{4+}@PDMS scintillator screen demonstrate its excellent imaging capabilities, with an observed resolution limit of 10 lp mm^{-1} (Fig. 5f). By using the modulation transfer function (MTF) based on the slanted-edge method, the spatial resolution at MTF = 0.2 was further determined to be 10 lp mm^{-1} (Fig. 5g and formula (S10)), which is similar to the imaging results of the standard X-ray resolution test panels. The light yield, detection limit, spatial resolution, and flexibility of the materials synthesized in this work rank at a relatively high level compared to related studies, and the comparison of key parameters is presented in Table S3.

The stability of halides is susceptible to degradation *via* deliquescence, and therefore the scintillator films were immersed in water for an extended period to characterize their stability in a humid environment. As shown in Fig. S6c, the prepared scintillator film retained over 86% of its initial intensity after remaining in water for one week, demonstrating that the PDMS provided substantial protection to the internal sample. Because the fabricated scintillation screen has excellent resolution, it is applied to X-ray imaging. The Cs_2ZrCl_6:Mo^{4+}@PDMS scintillation screen can absorb X-rays and convert them into light signals that are easy to observe. Objects made of different materials are placed between the X-ray and the scintillator screen. Different materials have different X-ray blocking capabilities, resulting in significant differences in the luminous intensity of the scintillator screen, which makes the internal structure of objects that are not visible to the naked eye clearly displayed in the imaging system. The imaging results showed that the metal components inside the phone card, the circuit

board, and the capsule that were invisible to the naked eye could be clearly displayed by the X-ray imaging system (Fig. 5h). The above results demonstrate that Cs_2ZrCl_6:Mo^{4+}@PDMS has excellent X-ray scintillation performance and has significant application potential in fields such as medical imaging, X-ray detection, and radiography.

4. Conclusions

In summary, we synthesized novel Mo^{4+} and W^{4+}-doped Cs_2ZrCl_6 as broadband NIR scintillators. The synthesized sample has the expected $Fm\bar{3}m$ vacancy-ordered double perovskite structure, with d^2 ions successfully doped into the lattice. The d^2 ion-doped sample exhibits broadband NIR luminescence and scintillation properties around 1000 nm. Cs_2ZrCl_6:Mo^{4+} has X-ray absorption capabilities comparable to commercial scintillators, with an LY of 51 613 photons MeV^{-1} and a detection limit as low as 192 nGy_{air} s^{-1}. Furthermore, an X-ray scintillation screen was fabricated by mixing Cs_2ZrCl_6:Mo^{4+} powder with PDMS. The prepared Cs_2ZrCl_6:Mo^{4+}@PDMS flexible films have outstanding imaging capability with spatial resolutions up to 10 lp mm^{-1}. The fabricated scintillator screen was successfully applied to X-ray imaging. This work demonstrates that d^2 ion-doped Cs_2ZrCl_6 is a promising material for X-ray imaging and detection with a wide range of applications.

Author contributions

Bing-Jun Zhu: data curation, software, visualization, writing – original draft, and writing – review and editing. Jiacheng Liu: validation. Yang (Michael) Yang: investigation. En Ma: methodology. Jia-Jun Yan: visualization. Heng-Yun Ye: conceptualization, funding acquisition, project administration, resources, and supervision. Le-Ping Miao: formal analysis.

Conflicts of interest

There are no conflicts to declare.

Data availability

The data supporting this article have been included as part of the supplementary information (SI). See DOI: **https://doi.org/10.1039/d6qm00065g**.

Acknowledgements

This work received support from the National Natural Science Foundation of China (22275075). E. Ma acknowledges the support of the Fujian STS Project (2024T3082).

References

1 Q. S. Chen, J. Wu, X. Y. Ou, B. L. Huang, J. Almutlaq, A. A. Zhumekenov, X. W. Guan, S. Y. Han, L. L. Liang, Z. G. Yi, J. Li, X. J. Xie, Y. Wang, Y. Li, D. Y. Fan, D. B. L. Teh, A. H. All, O. F. Mohammed, O. M. Bakr, T. Wu, M. Bettinelli, H. H. Yang, W. Huang and X. G. Liu, All-inorganic perovskite nanocrystal scintillators, *Nature*, 2018, **561**, 88–93.

2 X. Ouyang, R. Lin, Y. Ding, Y. Liang, W. Zheng, L. Chen, X. Song, F. Huang and X. Ouyang, Efficient sky-blue radioluminescence of microcrystalline $Cs_3Cu_2I_5$ based large-scale eco-friendly composite scintillators for high-sensitive ionizing radiation detection, *Mater. Chem. Front.*, 2021, **5**, 4739–4745.

3 H. Xu, W. Zhao, X. Zhang, J. Cui, Z. Wang, X. Liu, J. Shi and L. Ji, Flexible TADF-based organic X-ray scintillating films for high-resolution imaging, *Mater. Chem. Front.*, 2025, **9**, 480–486.

4 A. Elattar, A. Al Noman, A. Dyson, J. S. R. Vellore Winfred, B. Guzelturk, L. T. Kearney, A. M. Szucs and T. Dickens, 3D printed water-stable Cd-doped $Cs_4MnBi_2Cl_{12}$/polylactic acid perovskite/polymer composites for high-flux X-ray scintillation, *Mater. Chem. Front.*, 2026, **10**, 800–810.

5 Y. Zhou, Z. Wang, L. Guo, L. Huang, Y. Liu, M. Wu, Q. Zhang, K. An, P. He, F. Wang, J. Du, Z. Liu, Z. Hu, Y. Leng, Y. Pu, J. a Lai and X. Tang, Ultrafast and high-resolution X-ray imaging based on zero-dimensional organic silver halides, *Mater. Chem. Front.*, 2024, **8**, 3004–3016.

6 W. Wolszczak, K. W. Krämer and P. Dorenbos, CsBa2I5: Eu2+,Sm2+-The First High-Energy Resolution Black Scintillator for γ-Ray Spectroscopy, *Phys. Status Solidi RRL*, 2019, **13**, 1900158.

7 Y. D. Li, L. Q. Ge, S. Kun, G. Q. Zeng and R. Huang, Energy spectrum response of a CsI(TI) detector read out by an APD, *J. Instrum.*, 2020, **15**, T05005.

8 P. Ran, L. Yang, J. Hui, Y. Su, Z. Chen, H. Zhu, C. Kuang, X. Liu and Y. Yang, Single-shot X-ray and near-infrared (NIR) dual-mode fusion imaging based on bifunctional NIR scintillators, *Light: Sci. Appl.*, 2025, **14**, 315.

9 C. Wang, J. Xiao, S. Ma, Y. Li and Z. Yan, Efficient Near-Infrared Emitting Halide Scintillators with Mitigating External Light Crosstalk for Portable X-Ray Imaging, *Adv. Funct. Mater.*, 2024, **34**, 2401995.

10 D. Liu, P. Dang, G. Zhang, H. Lian, G. Li and J. Lin, Near-infrared emitting metal halide materials: Luminescence design and applications, *InfoMat*, 2024, **6**, e12542.

11 H. Wang, C. Peng, M. Chen, Y. Xiao, T. Zhang, X. Liu, Q. Chen, T. Yu and W. Huang, Wide-Range Color-Tunable Organic Scintillators for X-Ray Imaging Through Host-Guest Doping, *Angew. Chem., Int. Ed.*, 2024, **63**, e202316190.

12 J. Xu, R. Luo, Z. Luo, J. Xu, Z. Mu, H. Bian, S. Y. Chan, B. Y. H. Tan, D. Chi, Z. An, G. Xing, X. Qin, C. Gong, Y. Wu and X. Liu, Ultrabright molecular scintillators enabled by lanthanide-assisted near-unity triplet exciton recycling, *Nat. Photonics*, 2025, **19**, 71–78.

13 F. Zhang, Y. Zhou, Z. Chen, M. Wang, Z. Ma, X. Chen, M. Jia, D. Wu, J. Xiao, X. Li, Y. Zhang, Z. Shi and C. Shan, Thermally Activated Delayed Fluorescence Zirconium-Based Perovskites for Large-Area and Ultraflexible X-ray Scintillator Screens, *Adv. Mater.*, 2022, **34**, 2204801.

14 S. Cheng, M. Nikl, A. Beitlerova, R. Kucerkova, X. Du, G. Niu, Y. Jia, J. Tang, G. Ren and Y. Wu, Ultrabright and Highly Efficient All-Inorganic Zero-Dimensional Perovskite Scintillators, *Adv. Opt. Mater.*, 2021, **9**, 2100460.
15 Y. H. Chen, S. C. Liu, N. Zhou, N. X. Li, H. P. Zhou, L. D. Sun and C. H. Yan, An overview of rare earth coupled lead halide perovskite and its application in photovoltaics and light emitting devices, *Prog. Mater. Sci.*, 2021, **120**, 100737.
16 Y. Liu, X. M. Rong, M. Z. Li, M. S. Molokeev, J. Zhao and Z. G. Xia, Incorporating Rare-Earth Terbium(III) Ions into Cs2AgInCl6:Bi Nanocrystals toward Tunable Photoluminescence, *Angew. Chem., Int. Ed.*, 2020, **59**, 11634–11640.
17 K. A. Dagnall, A. M. Conley, L. U. Yoon, H. S. Rajeev, S.-H. Lee and J. J. Choi, Ytterbium-Doped Cesium Lead Chloride Perovskite as an X-ray Scintillator with High Light Yield, *ACS Omega*, 2022, **7**, 20968–20974.
18 Z. Liu, X. Qin, Q. H. Chen, Q. S. Chen, Y. H. Jing, Z. H. Zhou, Y. S. Zhao, J. S. Chen and X. G. Liu, Highly Stable Lead-Free Perovskite Single Crystals with NIR Emission Beyond 1100 nm, *Adv. Opt. Mater.*, 2022, **10**, 2201254.
19 W. Liao, K. Han, Y. Wang and Z. Xia, Cs_2HfCl_6:Mo^{4+} as Near-Infrared-Emitting Scintillators for Dual-Mode Collaborative Imaging, *Laser Photonics Rev.*, 2025, **19**, 2500311.
20 S. Saikia, A. Gopal, R. Rathod, A. Joshi, K. R. Priolkar, S. Saha, P. K. Santra, K. Shanmuganathan and A. Nag, Ultrabroad Near Infrared Emitting Perovskites, *Angew. Chem., Int. Ed.*, 2025, **64**, e202415003.
21 B. Yang, L. Yin, G. Niu, J.-H. Yuan, K.-H. Xue, Z. Tan, X.-S. Miao, M. Niu, X. Du, H. Song, E. Lifshitz and J. Tang, Lead-Free Halide Rb_2CuBr_3 as Sensitive X-Ray Scintillator, *Adv. Mater.*, 2019, **31**, 1904711.
22 Z. Wang, X. Xu, S. Wang, H. Xu, W. Xu, Q. Zeng, G. Deng, Y. Jiang and S. Wu, Cerium Doping Double Perovskite Scintillator for Sensitive X-ray Detection and Imaging, *Chem. - Eur. J.*, 2021, **27**, 9071–9076.
23 W. Ma, T. Jiang, Z. Yang, H. Zhang, Y. Su, Z. Chen, X. Chen, Y. Ma, W. Zhu, X. Yu, H. Zhu, J. Qiu, X. Liu, X. Xu and Y. Yang, Highly Resolved and Robust Dynamic X-Ray Imaging Using Perovskite Glass-Ceramic Scintillator with Reduced Light Scattering, *Adv. Sci.*, 2021, **8**, 2003728.
24 J. Sun, W. Zheng, P. Huang, M. Zhang, W. Zhang, Z. Deng, S. Yu, M. Jin and X. Chen, Efficient Near-Infrared Luminescence in Lanthanide-Doped Vacancy-Ordered Double Perovskite Cs2ZrCl6 Phosphors via Te4+ Sensitization, *Angew. Chem., Int. Ed.*, 2022, **61**, e202201993.
25 S. Liu, B. Yang, J. Chen, D. Wei, D. Zheng, Q. Kong, W. Deng and K. Han, Efficient Thermally Activated Delayed Fluorescence from All-Inorganic Cesium Zirconium Halide Perovskite Nanocrystals, *Angew. Chem., Int. Ed.*, 2020, **59**, 21925–21929.
26 W. Zhang, W. Zheng, L. Li, P. Huang, Z. Gong, Z. Zhou, J. Sun, Y. Yu and X. Chen, Dual-Band-Tunable White-Light Emission from Bi3+/Te4+ Emitters in Perovskite-Derivative Cs2SnCl6 Microcrystals, *Angew. Chem., Int. Ed.*, 2022, **61**, e202116085.
27 R. Shannon, Revised effective ionic radii and systematic studies of interatomic distances in halides and chalcogenides, *Acta Crystallogr., Sect. A*, 1976, **32**, 751–767.
28 S. Kumar, R. S. Lamba, S. Monga, V. Jha, S. Saha, S. Bhattacharya and S. Sapra, Broad Dual Emission from $Cs_2Zr_{1-x}Mo_xCl_6$: Enhancing the NIR Emission in Lead-free Vacancy Ordered Double Perovskites, *Chem. Mater.*, 2024, **36**, 4561–4570.
29 Z. Li, M. Xu, W. Liu, X. Wang, Y. Li, X. Zhou, Z. Fang and L. Ning, Broadband Near-Infrared Luminescence from Mo^{4+} in Zero-Dimensional Perovskite $Cs_2Zr(Cl,Br)_6$ with an Exceptionally High Quantum Efficiency and Thermal Stability, *Chem. Mater.*, 2024, **36**, 901–910.
30 B. Mondal, A. Shinde, P. K. Rajput, H. Arfin, R. Tanwar, P. Ghosh and A. Nag, Vibronically Coupled Near-Infrared Emission and Excitation from d-d Transitions of Cs_2MX_6 (M = Mo/W, X = Cl/Br), *ACS Energy Lett.*, 2024, **9**, 819–828.
31 S. Jin, R. Li, H. Huang, N. Jiang, J. Lin, S. Wang, Y. Zheng, X. Chen and D. Chen, Compact ultrabroadband light-emitting diodes based on lanthanide-doped lead-free double perovskites, *Light:Sci. Appl.*, 2022, **11**, 52.
32 B. Chen, Y. Guo, Y. Wang, Z. Liu, Q. Wei, S. Wang, A. L. Rogach, G. Xing, P. Shi and F. Wang, Multiexcitonic Emission in Zero-Dimensional Cs_2ZrCl_6:Sb^{3+} Perovskite Crystals, *J. Am. Chem. Soc.*, 2021, **143**, 17599–17606.
33 Y. Tanabe and S. Sugano, On the Absorption Spectra of Complex Ions. I, *J. Phys. Soc. Jpn.*, 1954, **9**, 753–766.
34 Y. Tanabe and S. Sugano, On the Absorption Spectra of Complex Ions II, *J. Phys. Soc. Jpn.*, 1954, **9**, 766–779.
35 Y. Tanabe and S. Sugano, On the Absorption Spectra of Complex Ions, III The Calculation of the Crystalline Field Strength, *J. Phys. Soc. Jpn.*, 1956, **11**, 864–877.
36 Y. Tanabe and H. Kamimura, On the Absorption Spectra of Complex Ions IV. The Effect of the Spin-orbit Interaction and the Field of Lower Symmetry on d electrons in Cubic Field, *J. Phys. Soc. Jpn.*, 1958, **13**, 394–411.
37 L. Marciniak, K. Kniec, K. Elzbieciak-piecka, K. Trejgis, J. Stefanska and M. Dramicanin, Luminescence thermometry with transition metal ions. A review, *Coord. Chem. Rev.*, 2022, **469**, 214671.
38 F. Zhang, Y. Zhou, Z. Chen, X. Niu, H. Wang, M. Jia, J. Xiao, X. Chen, D. Wu, X. Li, Z. Shi and C. Shan, Large-Area X-Ray Scintillator Screen Based on Cesium Hafnium Chloride Microcrystals Films with High Sensitivity and Stability, *Laser Photonics Rev.*, 2023, **17**, 2200848.
39 V. B. Mykhaylyk, M. Rudko, H. Kraus, V. Kapustianyk, V. Kolomiets, N. Vitoratou, Y. Chornodolskyy, A. S. Voloshinovskii and L. Vasylechko, Ultra-fast low temperature scintillation and X-ray luminescence of $CsPbCl_3$ crystals, *J. Mater. Chem. C*, 2023, **11**, 656–665.
40 S. Yan, S. Liu, Z. Teng, H. Li, W. Chen, W. Zhou, J. Qiu, X. Yu, S. Wang and X. Xu, High quality lead-free perovskites toward white light emitting diodes and X-ray imaging, *J. Mater. Chem. C*, 2022, **10**, 16294–16300.
41 W. Ma, Y. Su, Q. Zhang, C. Deng, L. Pasquali, W. Zhu, Y. Tian, P. Ran, Z. Chen, G. Yang, G. Liang, T. Liu, H. Zhu, P. Huang, H. Zhong, K. Wang, S. Peng, J. Xia, H. Liu, X. Liu and Y. Yang, Thermally activated delayed fluorescence (TADF) organic molecules for efficient X-ray scintillation and imaging, *Nat. Mater.*, 2022, **21**, 210–216.

42 R. Liu, W. Zhang, G. Li and W. Liu, An ultraviolet excitation anti-counterfeiting material of Sb^{3+} doped Cs_2ZrCl_6 vacancy-ordered double perovskite, *Inorg. Chem. Front.*, 2021, **8**, 4035–4043.

43 M. J. Berger, J. H. Hubbell, S. M. Seltzer, J. S. Chang, J. S. Coursey, R. Sukumar, D. S. Zucker and K. Olsenk, XCOM: Photon Cross Sections Database 2010, **https://www.nist.gov/pml/xcom-photon-cross-sections-database**, 2010, DOI: **10.18434/T48G6X**.

44 H. Xu, W. Liang, Z. Zhang, C. Cao, W. Yang, H. Zeng, Z. Lin, D. Zhao and G. Zou, 2D Perovskite Mn^{2+}-Doped $Cs_2CdBr_2Cl_2$ Scintillator for Low-Dose High-Resolution X-ray Imaging, *Adv. Mater.*, 2023, **35**, 2300136.

45 Z. Tan, J. Pang, G. Niu, J.-H. Yuan, K.-H. Xue, X. Miao, W. Tao, H. Zhu, Z. Li, H. Zhao, X. Du and J. Tang, Tailoring the electron and hole dimensionality to achieve efficient and stable metal halide perovskite scintillators, *Nanophotonics*, 2021, **10**, 2249–2256.

46 Q. Zhou, J. Ren, J. Xiao, L. Lei, F. Liao, H. Di, C. Wang, L. Yang, Q. Chen, X. Yang, Y. Zhao and X. Han, Highly efficient copper halide scintillators for high-performance and dynamic X-ray imaging, *Nanoscale*, 2021, **13**, 19864–19902.